Mechanism and Machine Theory 217 (2025) 106266

Contents lists available at ScienceDirect

Mechanism and Machine Theory

journal homepage: www.elsevier.com/locate/mechmt

Research paper

On the lumped parameter modeling of worm gear mechanisms: Experimental validation and insights

Giulia Cristofori *, Mattia Battarra, Emiliano Mucchi

University of Ferrara, Engineering Dept., Via G. Saragat, 1 - 44121 Ferrara, Italy

ARTICLE INFO

Keywords:
Worm gear
Lumped parameter model
Meshing stiffness

ABSTRACT

A non-linear 8-DOF model capable of capturing the fundamentals of the worm gear dynamics has been developed. The model incorporates external excitations, non-linear time-varying meshing stiffness, and components related to friction phenomena. This study is dedicated to a thorough exposition of the lumped parameter model, accompanied by a comprehensive examination of its equations and an analysis of the impact of diverse contributions. The procedure employed to determine the meshing stiffness is further investigated using a finite element methodology, as it is a crucial input for the dynamic model. Furthermore, a comprehensive description of the experimental campaign conducted to validate the model is presented, enabling an in-depth analysis of the impact of speed and torque on the overall dynamics of worm gear mechanisms. In order to assess the capability of the model to accurately capture the effects of these two parameters, a comparison is made between the numerical results, specifically the bearing forces and transmission errors, and the experimental data. These comparisons facilitate the validation of the model.

1. Introduction

Worm gears have a unique property: the worm can drive the gear, but not vice versa, due to the shallow angle and resulting friction that prevents backdriving. This makes them ideal for holding loads in position without continuous motor actuation. Their non-backdrivability, high transmission ratios, and compact size make them common in electromechanical systems, especially when torque redirection is needed. This study aims to develop a robust lumped parameter model of worm gear systems to extend theoretical understanding. Accurate modeling is essential for optimizing performance and analyzing parameter effects, reducing the need for costly, time-consuming experiments. In the context of this study, a review of the literature reveals several works focused on lumped parameter modeling of gear systems, such as spur gears and gear pumps [1,2]. However, there is still a considerable amount of work to be done on the modeling of more complicated gear systems, such as the worm gear systems. Recently, researchers have increasingly focused their efforts on modeling and controlling worm gear systems to significantly improve their performance. Central to these models are two critical factors: friction and mesh stiffness, which play a pivotal role in accurately predicting system behavior. Despite their importance, these two elements remain subjects of ongoing debate in the literature, with various approaches being proposed by different authors. As a result, a universally accepted method for their incorporation remains to be established, emphasizing the necessity for further exploration in this domain.

Within the context of worm gear modeling, Mooring et al. [3] and May et al. [4] pioneered the development of a 2-DOFs model for a robot joint, incorporating a worm gear transmission. Notably, their work laid the foundation for subsequent analyses, although

---

* Corresponding author.
E-mail address: crsgli1@unife.it (G. Cristofori).

https://doi.org/10.1016/j.mechmachtheory.2025.106266
Received 2 May 2025; Received in revised form 17 September 2025; Accepted 15 October 2025

Nomenclature

Acronyms

CCW	Counter-clockwise
CW	Clockwise
DOF	Degrees of freedom
DTC	Double tooth contact
FE	Finite element
IAS	Instantaneous angular speed
LP	Lumped parameter
ppr	Pulse per revolution
TSA	Time synchronous average
TTC	Triple tooth contact

Greek symbols

α	Rayleigh's damping mass proportionality coefficient
β	Rayleigh's damping stiffness proportionality coefficient
$\ddot{\theta}_i$	Angular acceleration of body i
$\dot{\theta}_i$	Angular velocity of body i
λ	Lead angle
μ	Friction coefficient
$\overline{\theta}_i$	Mean tangential displacement of the FE model for body i
$\boldsymbol{\Phi}_n$	Normal pressure angle
θ_i	Angular displacement of body i
θ_p	Angular pitch
ζ	Damping ratio

Latin symbols

$\ddot{x}_i$	Radial acceleration in the x-direction for body i
$\ddot{y}_i$	Radial acceleration in the y-direction for body i
$\ddot{z}_i$	Radial acceleration in the z-direction for body i
$\dot{x}_i$	Radial velocity in the x-direction for body i
$\dot{y}_i$	Radial velocity in the y-direction for body i
$\dot{z}_i$	Radial velocity in the z-direction for body i
$\hat{\mathbf{x}}$	Unit vector representing the x-direction
$\hat{\mathbf{y}}$	Unit vector representing the y-direction
$\hat{\mathbf{z}}$	Unit vector representing the z-direction
$\overline{u}_{\theta,i}$	Mean tangential deflection of the FE model for body i
$\overline{x}_i$	Average displacement values between all nodes of the FE model in the x-direction for body i
$\overline{x}_r$	Transmission error evaluated considering the averaged displacements between all nodes of the FE model
$\overline{y}_i$	Average displacement values between all nodes of the FE model in the y-direction for body i
$\overline{z}_i$	Average displacement values between all nodes of the FE model in the z-direction for body i
$\mathbf{C}$	Damping matrix
$\mathbf{f}_e$	Vector containing the external forces
$\mathbf{f}_f$	Vector containing the friction forces
$\mathbf{K}$	Stiffness matrix
$\mathbf{K}_f$	Matrix containing the cosine director related to the friction forces
$\mathbf{M}$	Mass matrix
$\mathbf{n}_i$	Vector representing the direction of the meshing forces between teeth for body i
$\mathbf{q}$	Vector containing the degrees of freedom of the model
$\mathbf{t}_i$	Vector representing the direction of the friction forces between teeth for body i
$\tilde{x}(\theta)$	Time synchronous average in angular domain

$\tilde{X}(O)$	Time synchronous average spectrum in order domain
C_H	Coefficient which denotes if the mechanism is left hand or right hand
C_R	Coefficient which denotes if the mechanism rotates CW or CCW
F_b	Bearing forces
$f_{e,i}^{x}$	External forces in the x-direction for body i
$f_{e,i}^{y}$	External forces in the y-direction for body i
$f_{e,i}^{z}$	External forces in the z-direction for body i
J_i	Mass moment of inertia of body i
k_t	Torsional stiffness
$k_{bi,x}$	Bearing stiffness related to body i in the x-direction
$k_{bi,y}$	Bearing stiffness related to body i in the y-direction
$k_{bi,z}$	Bearing stiffness related to body i in the z-direction
k_b	Bearing stiffness
k_m	Worm gear mesh stiffness
k_t	Torsional stiffness
m	Standard module
m_i	Mass of body i
O	Order
R_i	Base radius of body i
$r_{FE,i}$	Radii of the FE model where the results are computed for body i
T	Torque
t	Time vector
$T_{e,i}$	External torque on body i
$x(\theta)$	Signal in angular domain
$x(t)$	Signal in time domain
x_i	Radial displacement in the x-direction for body i
x_r	Transmission error
y_i	Radial displacement in the y-direction for body i
Z_i	Number of teeth of gear i
z_i	Radial displacement in the z-direction for body i

Subscripts

e	Denotes the components related to external components
f	Denotes the components related to friction
g	Denotes the gear
i	Denotes the body i which can be either the helical gear or the worm
w	Denotes the worm
$axial$	Denotes the axial component
$radial$	Denotes the radial component

factors like gear backlash and time-varying meshing stiffness are not considered. Chung et al. [5] advanced the modeling approach by proposing a 2-DOFs model that accounted for additional factors, including friction force and elastic deformation of gear teeth. Their findings revealed that these factors significantly contribute to rotational positioning errors, introducing an understanding of the impact of various parameters on system performance. Brown et al. [6] extended the scope to encompass robot arms and unmanned ground vehicles, introducing a non-backdrivable worm gear model with two DOFs and a static Direct Current motor. Their model demonstrated a significant reduction in the maximum required torque and consumed energy, highlighting the potential efficiency gains achievable through sophisticated modeling. Bordegaray et al. [7] elevated the complexity by introducing a model with 6-DOFs, including translational degrees of freedom. Notably, they addressed non-linearities arising from backlash using a variable meshing stiffness approximated by a continuous function. However, the model did not consider the friction coefficient, which requires further refinement to fully understand the dynamics of the system. Benabid et al. [8] expanded the model to 8-DOFs, incorporating the friction coefficient into the dynamic analysis but excluding consideration of the time-varying meshing stiffness. Chakroun et al. utilized the same 8-DOF model, as described in [9], to explore the dynamic behavior of a worm gear mechanism. The investigation encompassed both metal–metal and polymer–metal worm gears. Hammami et al. [10] increased the complexity to 14-DOFs while retaining the meshing stiffness approach from [11]. Their study highlighted the influence of material softening and increased friction coefficient on vibration amplitudes, although experimental validation was not conducted.

Liu et al. [12] contributed a comprehensive 8-DOF bending-twisting shaft coupling dynamic model. This model considered critical factors such as time-varying meshing stiffness, tooth meshing error, and meshing damping. Liu's work provided valuable insights into the influence of machining accuracy, modification amount, and assembly errors on vibration characteristics, with experimental validation conducted on a specialized test bench.

As mention before, it is worth noting that the precise modeling of the friction phenomena plays a pivotal role in the modeling of worm gear mechanisms, given the significant impact of friction within these systems. However, it has been observed that not all extant models take this phenomenon into consideration. Regarding the influence of the friction coefficient and its measurement, Shin et al. [13] and Kim et al. [14] conducted extensive measurements of the friction coefficient using a tribometer, taking into account variables such as normal pressure and sliding velocity. The research offers valuable insights into the complex relationship between friction and operational parameters. Noteworthy is the emphasis by Garcia et al. [15] on the significance of meshing friction, particularly at lower speeds, highlighting the necessity for precise modeling in systems characterized by slow-motion dynamics. In response, they introduced a model of meshing friction that explicitly considers variations in sliding velocity. Li et al. [16] adopted the LuGre model [17] to approach friction coefficient modeling. This modeling framework suggests a comprehensive consideration of friction characteristics, aiming to capture the friction behavior within the context of worm gear mechanisms. Sesana and Sadeghi [18] took a theoretical approach to evaluate the friction coefficient, applying the results to model the friction in the steering system. Addressing the practical implications, Gao et al. [19] emphasized the impact of the friction coefficient on meshing efficiency. Their findings underscore the necessity of enhancing lubrication conditions between meshing tooth surfaces in practical applications.

Similarly, a universally accepted modeling of mesh stiffness is lacking, and the majority of commercial software for the design of such systems does not permit the estimation of mesh stiffness through accurate contact analysis. Nevertheless, the assessment of meshing stiffness in this mechanism holds significant importance in achieving an accurate prediction of real dynamic behavior, given its pivotal role as the primary internal excitation source for dynamic responses in gears. Several studies have investigated the contact area of meshing, using both analytical [20–23] and numerical approaches [24–29]. These studies examined the effects of various parameters, including tooth errors, shaft misalignments [30,31], and mismatched gearing [32,33]. Hiltcher et al. [34] contributed a method that extends Kelvin's model, offering a comprehensive exploration into the impact of temperature and rotational speed on transmission error and meshing stiffness in a steel worm and a nylon wheel. The study by Chakroun et al. [35] further delves into the behavior of polymer–metal worm gears, employing the Generalized Maxwell rheological model to compute gear meshing stiffness. Liu et al. [36] conducted a comparative analysis of gear meshing stiffness in a plastic helical gear metal worm drive, utilizing both analytical methodologies and finite element models to validate accuracy. However, all the aforementioned works do not involve the modeling of the actual contact mechanism between the worm and the gear. Indeed, by taking into account a polymer gear meshing with a metal worm, these studies assume the stiffness of the worm as negligible and lead to the hypothesis that the mesh stiffness coincides with the tooth bending stiffness of the polymer gear, which is a parameter that can be straightforwardly provided by several commercial softwares. As a matter of fact, in the event that one of the two gears exhibits a stiffness that is significantly lower than the other, it is feasible to omit the calculation of the gear with higher stiffness. Therefore, while the aforementioned approaches provide valuable insights into plastic-metal worm gears, they cannot be used to analyze metal-to-metal worm gears as well as plastic-to-plastic worm gears. In order to overcome these limitations, the present work takes advantage of the methodology proposed by Cooley et al. in [37] for the spur gear meshing stiffness estimation in a 2D environment and extended it to worm gear systems in a 3D environment. The validity of the proposed procedure is substantiated by the findings of the LP model validated against experimental determination of the dynamic transmission error.

By integrating advanced numerical modeling techniques with rigorous experimental validation, this research aims to enhance the predictive capabilities of worm gear models. In this study, an 8-DOFs lumped parameter model of worm gear mechanisms is developed. The model is derived from the description of the equations that govern the system. This incorporates time-varying load-dependent meshing stiffness, non-linear damping effects, and friction phenomena, enabling a detailed analysis of gear behavior under operational conditions. As an innovative aspect, the developed model is capable of solving both the CW and CCW rotations as well as the right-hand and the left-hand conditions. Moreover, to address the gap in the existing literature, a finite element methodology based on Cooley's approach is developed for assessing the worm gear meshing stiffness. This methodology takes into account the dependency on the percentage of angular pitch and the applied load, deriving a time-varying meshing stiffness. A further investigation is conducted to evaluate the contribution of each DOF to the transmission error. This investigation was undertaken to achieve a more profound comprehension of the mechanism dynamics. Furthermore, both proportional viscous damping and friction phenomena are taken into consideration, and an analysis of these contributions is conducted to understand the influence of these on the model dynamics. The robustness of the model is confirmed through the experimental validation, which is performed using high-precision measurement systems to capture both the transmission errors and the vibration characteristics. The results are then compared with numerical predictions to assess the accuracy of the model by encompassing a wider range of data, considering tests with different torques and velocities and validating both the translational and the rotational DOFs.

The following Section (Section 2) is devoted to the description of the model equations used for the analysis of the worm gear dynamics. Section 3 describes the finite element methodology to define the meshing stiffness, delving into the components that contribute to the definition of the meshing stiffness. In Section 4, the experimental campaign is accurately described. The model results are reported in Section 4, comprising the validation results and the sensitivity analysis. Concluding remarks are reported in Section 5.

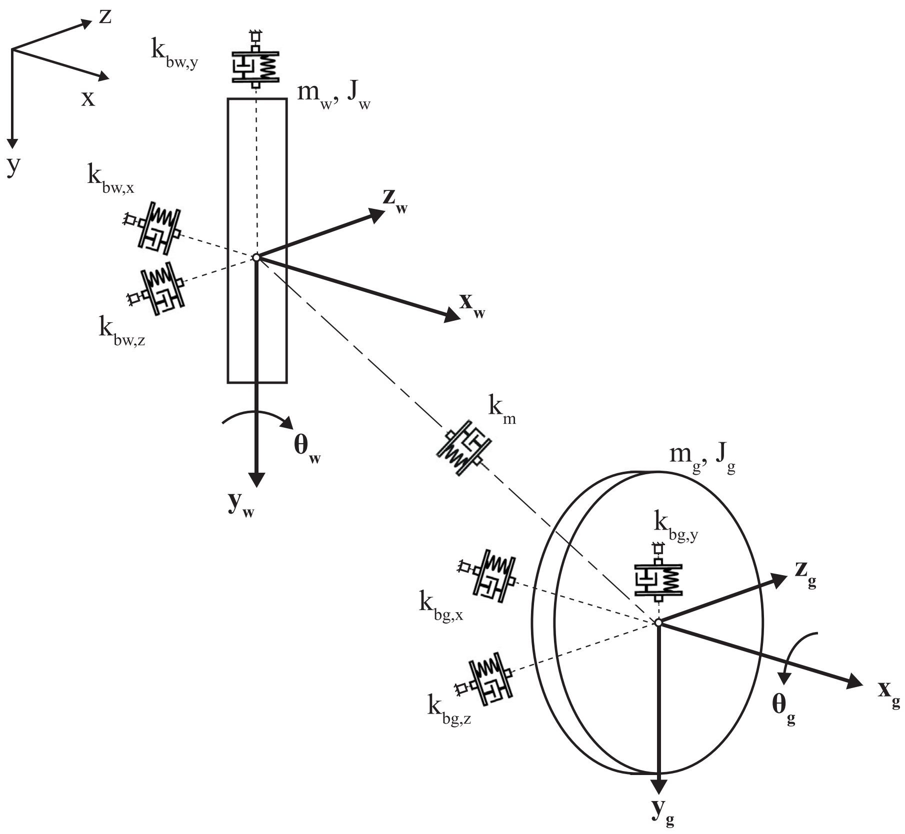

Fig. 1. Lumped parameter model of the worm gear system.

2. Dynamic model

This section provides a comprehensive overview of the model system equations, meticulously analyzing the components that are pivotal to the dynamics of the system. As illustrated in Fig. 1, the three-dimensional configuration of the mechanism under investigation consists of a worm and a helical gear. Both the worm and the gear are considered to have three translational degrees of freedom in the x, y, and the z directions, denoted by x_i, y_i, and z_i in the model equations. The subscripts w and g refer to the worm and the gear, respectively. The rotational DOFs are defined with respect to the axis of rotation of the two considered bodies. Therefore, according to the reference frame, θ_w represents the rotation around the y-axis, and θ_g represents the rotation around the x-axis. It is assumed that the rotational degrees of freedom in the non-axial directions of the worm and the gear are negligible. As a support of that, Benabid et al. [8] and Liu et al. [12] validated 8-DOF models against experimental data, showing that this level of complexity is sufficient to accurately describe the system dynamics while maintaining model simplicity. Moreover, it is worth noting that the gears are mounted on rolling bearings so both radial ($k_{bw,x}$ and $k_{bw,z}$ for the worm and $k_{bg,y}$ and $k_{bg,z}$ for the gear) and axial stiffness ($k_{bw,y}$ for the worm and $k_{bg,x}$ for the gear) components of the bearings are considered. The equation describing the system dynamics may be written as follows:

$$\mathbf{M}\,\ddot{\mathbf{q}} + \mathbf{C}\,\dot{\mathbf{q}} + \mathbf{K}\,\mathbf{q} + \mathbf{f}_f = \mathbf{f}_e \tag{1}$$

where $\mathbf{q}$ is the vector containing the eight degrees of freedom considered in the model, exploited in Eq. (2).

$$\mathbf{q} = \left\{ x_w \quad y_w \quad z_w \quad \theta_w \quad x_g \quad y_g \quad z_g \quad \theta_g \right\}^T \tag{2}$$

The subscript w is used to denote the worm, while the subscript g is used to denote the gear. The translational degrees of freedom are designated by x, y and z, while the rotational ones are denoted by θ for both the worm and the gear. $\mathbf{M}$ is the mass matrix,

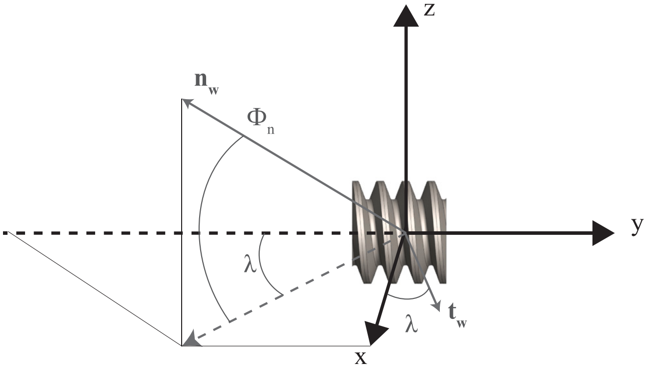

Fig. 2. Unity vector of the meshing force and the friction force from the worm to the gear in the case of right-hand mechanism.

Table 1
Constants for the model equations.

	Right Hand CW	Right Hand CCW	Left Hand CW	Left Hand CCW
C_R	1	–1	1	–1
C_H	1	1	–1	–1

whose elements are described in Eq. (3), which contains m_i and J_i, i.e. mass and polar inertia, respectively.

$$\mathbf{M} = \begin{bmatrix} m_w & 0 & 0 & 0 & 0 & 0 & 0 & 0 \\ 0 & m_w & 0 & 0 & 0 & 0 & 0 & 0 \\ 0 & 0 & m_w & 0 & 0 & 0 & 0 & 0 \\ 0 & 0 & 0 & J_w & 0 & 0 & 0 & 0 \\ 0 & 0 & 0 & 0 & m_g & 0 & 0 & 0 \\ 0 & 0 & 0 & 0 & 0 & m_g & 0 & 0 \\ 0 & 0 & 0 & 0 & 0 & 0 & m_g & 0 \\ 0 & 0 & 0 & 0 & 0 & 0 & 0 & J_g \end{bmatrix} \tag{3}$$

While $\mathbf{f_e}$ is the vector that contains the external forces (Eq. (4)).

$$\mathbf{f_e} = \left\{ f^x_{e,w} \quad f^y_{e,w} \quad f^z_{e,w} \quad T_{e,w}/R_w \quad f^x_{e,g} \quad f^y_{e,g} \quad f^z_{e,g} \quad T_{e,g}/R_g \right\}^T \tag{4}$$

The damping matrix has been expressed as a result of adopting the Rayleigh damping model:

$$\mathbf{C} = \alpha\mathbf{M} + \beta\mathbf{K} \tag{5}$$

where α is the Rayleigh's damping mass proportionality coefficient and β the Rayleigh's damping stiffness proportionality coefficient. The selection of α and β is based on the authors′ experience and experimental data available in the literature [9,12]. This approach is considered more reliable than defining all components of the damping matrix directly. Moreover, the Rayleigh formulation ensures viscous-type damping, which is characteristic of gear transmission systems. The definition of the stiffness matrix, denoted by **K**, requires further elaboration. Considering the reference system in Fig. 1, it is imperative to define the vector of the meshing forces. In order to clarify the system architecture, Fig. 2 illustrates the unit vector ($\mathbf{n_w}$) of the forces exchanged between teeth under right-hand CW conditions with reference to the absolute reference system. Adopting this approach, the components of the meshing unit vector are expressed in Eq. (6), incorporating the right-hand and left-hand mechanisms, as well as clockwise (CW) and counter-clockwise (CCW) rotations. The configurations of these rotations are not shown in the scheme in Fig. 2 for the sake of brevity.

$$\mathbf{n_w} = \begin{cases} cos\Phi_n sin\lambda\hat{\mathbf{x}} - cos\Phi_n cos\lambda\hat{\mathbf{y}} + sin\Phi_n\hat{\mathbf{z}} & \text{if Right Hand CW} \\ -cos\Phi_n sin\lambda\hat{\mathbf{x}} + cos\Phi_n cos\lambda\hat{\mathbf{y}} + sin\Phi_n\hat{\mathbf{z}} & \text{if Right Hand CCW} \\ cos\Phi_n sin\lambda\hat{\mathbf{x}} + cos\Phi_n cos\lambda\hat{\mathbf{y}} + sin\Phi_n\hat{\mathbf{z}} & \text{if Left Hand CW} \\ -cos\Phi_n sin\lambda\hat{\mathbf{x}} - cos\Phi_n cos\lambda\hat{\mathbf{y}} + sin\Phi_n\hat{\mathbf{z}} & \text{if Left Hand CCW} \end{cases} \tag{6}$$

where Φ_n is the pressure angle and λ is the lead angle. The unity vector in the x, y and z-directions are represented by the symbols $\hat{x}$, $\hat{y}$ and $\hat{z}$.

Based on these considerations, the stiffness matrix for the meshing components is exploited in Eq. (7). The matrix elements have been generalized using coefficients to ensure applicability to all possible geometric and operational conditions. Within this scope, two parameters have been defined, namely C_H and C_R in Table 1. The use of these coefficients facilitates the generalization of the model, thereby enabling efficient transitions between all possible configurations. In the interest of achieving a more compact

Table 2
Coefficients for the model equations.

Parameters	Values
C_1	$cos\Phi_n sin\lambda$
C_2	$cos\Phi_n cos\lambda$
C_3	$sin\Phi_n$

representation, three supplementary parameters, designated C_1, C_2 and C_3 (see Table 2), have been delineated. These parameters encompass the cosine and sine directors of the model's equation.

$$\mathbf{K} = k_m(t, x_r)\begin{bmatrix}\mathbf{K_{11}} & \mathbf{K_{12}} \\ \mathbf{K_{21}} & \mathbf{K_{22}}\end{bmatrix} \tag{7}$$

The details of the meshing stiffness elements are summarized as follows:

$$\mathbf{K_{11}} = \begin{bmatrix} C_1^2 & -C_1C_2C_H & C_3C_1C_R & R_wC_1^2 \\ -C_1C_2C_H & C_2^2 & -C_3C_2C_RC_H & -R_wC_1C_2C_H \\ C_3C_1C_R & -C_3C_2C_RC_H & C_3^2 & R_wC_3C_1C_R \\ R_wC_1^2 & -R_wC_1C_2C_H & R_wC_3C_1C_R & R_w^2C_1^2 \end{bmatrix} \tag{8}$$

$$\mathbf{K_{12}} = \begin{bmatrix} -C_1^2 & C_1C_2C_H & -C_3C_1C_R & R_gC_1C_2C_H \\ C_1C_2C_H & -C_2^2 & C_3C_2C_RC_H & -R_gC_2^2 \\ -C_3C_1R & C_3C_2C_RC_H & -C_3^2 & R_gC_3C_2C_RC_H \\ -R_wC_1^2 & R_wC_1C_2C_H & -R_wC_3C_1C_R & R_wR_gC_1C_2C_H \end{bmatrix} \tag{9}$$

$$\mathbf{K_{21}} = \begin{bmatrix} -C_1^2 & C_1C_2C_H & -C_3C_1C_R & -R_wC_1^2 \\ C_1C_2C_H & -C_2^2 & C_3C_2C_RC_H & R_wC_1C_2C_H \\ -C_3C_1C_R & C_3C_2C_RC_H & -C_3^2 & -R_wC_3C_1C_R \\ R_gC_1C_2C_H & -R_gC_2^2 & R_gC_3C_2C_RC_H & R_wR_gC_1C_2C_H \end{bmatrix} \tag{10}$$

$$\mathbf{K_{22}} = \begin{bmatrix} C_1^2 & -C_1C_2C_H & C_3C_1C_R & -R_gC_1C_2C_H \\ -C_1C_2C_H & C_2^2 & -C_3C_2C_RC_H & R_gC_2^2 \\ C_3C_1C_R & -C_3C_2C_RC_H & C_3^2 & -R_gC_3C_2C_RC_H \\ -R_gC_1C_2C_H & R_gC_2^2 & -R_gC_3C_2C_RC_H & R_g^2C_2^2 \end{bmatrix} \tag{11}$$

It is important to note that the value of the meshing stiffness, as illustrated in Eq. (7), is contingent on both the time and the transmission error value, which formula is exploited in Eq. (12):

$$x_r(t) = C_1[x_w(t) - x_g(t) - R_w\theta_w(t)] + C_2[-y_w(t) + y_g(t) - R_g\theta_g(t)] + C_3[z_w(t) - z_g(t)] \tag{12}$$

As previously stated, this model also incorporates components related to the friction phenomenon, which is widely considered to be of high importance in such mechanisms. Within this context, the vector of friction forces ($\mathbf{f_f}$) represents the tangential forces resulting from the exchange of forces between the teeth in the tangential direction, i.e. $\mathbf{t_w}$ in Fig. 2. This is in consideration of the absolute reference frame, taking a right-hand mechanism in a clockwise rotation condition. The friction forces are described as follows:

$$\mathbf{f_f} = \mu\mathbf{K_f}\ \mathbf{q} \tag{13}$$

These components are intrinsically linked to the friction coefficient (μ), which is predicated on the mechanism under investigation. Since the directions of the friction forces are normal to the meshing forces, the matrix which contains the cosine director ($\mathbf{K_f}$) is given by the following expressions:

$$\mathbf{K_f} = k_m(t, x_r)\begin{bmatrix}\mathbf{K_{f,11}} & \mathbf{K_{f,12}} \\ \mathbf{K_{f,21}} & \mathbf{K_{f,22}}\end{bmatrix} \tag{14}$$

$$\mathbf{K_{f,11}} = \begin{bmatrix} C_1cos\lambda & -C_2cos\lambda C_H & 0 & R_wC_1cos\lambda \\ C_1sin\lambda C_H & -C_2sin\lambda & 0 & R_wC_1sin\lambda C_H \\ 0 & 0 & 0 & 0 \\ R_wC_1cos\lambda & -R_wC_2cos\lambda C_H & 0 & R_w^2C_1cos\lambda \end{bmatrix} \tag{15}$$

$$\mathbf{K_{f,12}} = \begin{bmatrix} -C_1cos\lambda & C_2cos\lambda C_H & 0 & R_gC_2cos\lambda \\ -C_1sin\lambda C_H & C_2sin\lambda & 0 & R_gC_2sin\lambda C_H \\ 0 & 0 & 0 & 0 \\ -R_wC_1cos\lambda & R_wC_2cos\lambda C_H & 0 & R_wR_gC_2cos\lambda \end{bmatrix} \tag{16}$$

$$\mathbf{K_{f,21}} = \begin{bmatrix} -C_1cos\lambda & C_2cos\lambda C_H & 0 & -R_wC_1cos\lambda \\ -C_1sin\lambda C_H & C_2sin\lambda & 0 & -R_wC_1sin\lambda C_H \\ 0 & 0 & 0 & 0 \\ -R_gC_1sin\lambda C_H & R_gC_2sin\lambda & 0 & -R_wR_gC_1sin\lambda C_H \end{bmatrix} \tag{17}$$

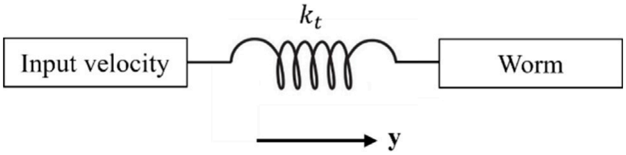

Fig. 3. Worm shaft modeling scheme.

$$\mathbf{K}_{\mathbf{f},22} = \begin{bmatrix} C_1 cos\lambda & -C_2 cos\lambda C_H & 0 & -R_g C_2 cos\lambda \\ C_1 sin\lambda C_H & -C_2 sin\lambda & 0 & -R_w C_2 sin\lambda C_H \\ 0 & 0 & 0 & 0 \\ R_g C_1 sin\lambda C_H & -R_g C_2 sin\lambda & 0 & -R_g^2 C_2 sin\lambda C_H \end{bmatrix} \tag{18}$$

It is worth noting that the friction contributions are null in the z-direction. Furthermore, an investigation into the matrix $\mathbf{K_f}$ has revealed that it is not symmetrical.

In the context of the simulation, the mechanical compliance of the worm shaft is also taken into consideration. This is achieved by incorporating a torsional stiffness, namely k_t, into the lumped parameter model. The purpose of this is to establish a connection between the input velocity and the lumped parameter mass of the worm. As illustrated in Fig. 3, the relative scheme is demonstrated. The torsional stiffness value is contingent on the mechanical properties of the worm shaft.

3. Meshing stiffness evaluation

This Section presents a method for computing the meshing stiffness of a worm gear, addressing the shortcomings of previous literature reviews. As a matter of fact, as these authors are aware, no methodologies are present in the literature for estimating the meshing stiffness between the worm and the gear when both are made of metal. Thus, the proposed methodology uses Cooley's pure FE methodology [37], which has been extended for application to worm gear mechanisms. The average slope approach is chosen for development, and all the FE analyses have been performed by the use of the Nastran solver.

The procedure for assessing the mesh stiffness commences with the three-dimensional model of the worm gear pair. At first, both bodies are simplified, aiming to reduce the computational time and the required memory. The reduction in the number of gear teeth was based on Natali et al. [38]. As shown in that study, the mesh stiffness results vary by an average of only 3% when reducing the model from the full geometry to configurations with reduced tooth pairs. This level of deviation is deemed acceptable given the significant computational savings achieved through geometric simplification. In particular, the gear is simplified by reducing the number of teeth from thirty to six. Furthermore, the model exclusively considers the geared component of the worm, with the remainder of the shaft being excluded for the purpose of analysis. It is noteworthy that analogous results are obtained when considering the entire mode. However, these results will not be presented here for the sake of brevity. In this study, a tetrahedral mesh was adopted based on convergence tests and prior validated models to balance accuracy and computational cost. While hexahedral meshes can offer advantages for stress analysis, generating a high-quality hex mesh is significantly more time-consuming, especially without specialized tools. As shown by Chakroun et al. [39], tetrahedral and hexahedral meshes yield similar displacement results, which are the focus of this work. Since stress was not evaluated, the tetrahedral mesh was considered adequate for our purposes. As illustrated in Fig. 4(a), the mesh consists of 3D tetrahedral elements with 10 nodes, with an average element dimension of 2 mm. The figure shows the initial contact point where only two teeth are in contact. Due to the non-linear nature of the finite element analysis, further refinement is necessary in the contact zone of the teeth. Refining the mesh in the contact region is critical for accurately estimating gear mesh stiffness in finite element (FE) models. Due to high stress gradients and localized deformations, coarse meshes fail to capture the nonlinear contact behavior. As demonstrated by Cooley et al. [37] and Natali et al. [38], a fine mesh is essential for obtaining reliable results, particularly in dynamic analyses employing the local stiffness approach. Within this framework, a surface refinement of the flanks where contact exists is performed, taking into account an element size of 0.3 mm. As illustrated in Fig. 4(b), the local enlarged view of the mesh is provided. In particular, as a means to reduce the computational time, the refinement process is confined exclusively to the part of the flank where contact is established. The dimensions of the elements are selected at the outset of a mesh convergence procedure, the results of which are not presented here for the sake of brevity. As illustrated in Fig. 5, the boundary conditions imposed on the FE model involve the application of a torque to a node located at the center of the worm body which is also connected to the worm hub by RBE2 (Rigid Body Element, Form 2) rigid elements. While the hub face of the gear has been constrained to prevent the rigid body from rotating. In order to simulate the contact between teeth, nonlinear contact elements are employed. The contact algorithm is based on the augmented Lagrange method. SOL 401 Multi-Step Nonlinear is implemented. Subsequent to the preparation of the model, a series of simulations is conducted at multiple angular positions. The objective of these simulations is to ascertain the mesh stiffness throughout a tooth mesh cycle. Specifically, the simulations are performed from 0% to 100% of the angular pitch, incorporating a total of twelve positions. Furthermore, several torque values have been considered for each angular position, with the purpose of characterizing the relation between the mesh stiffness and the transmission error of the system.

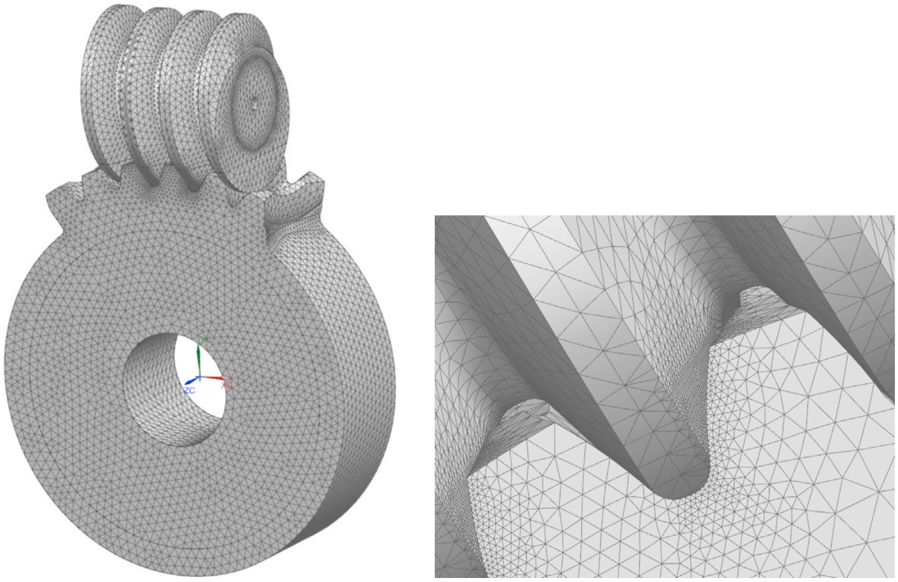

(a) Entire mesh.
(b) Local enlarged view.

Fig. 4. 3D mesh.

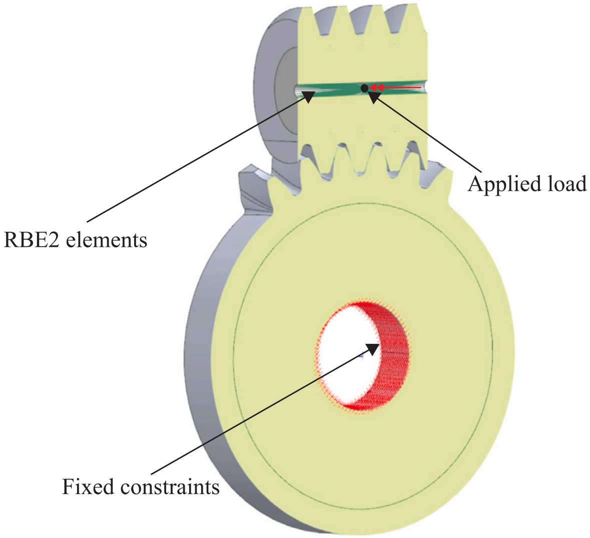

Fig. 5. Details of the FE model boundary conditions.

The procedure to obtain the mesh stiffness value, considering the average approach, is explained hereinafter. In particular, the meshing stiffness is defined in Eq. (19):

$$k_m = \frac{T}{R_w \overline{x}_r} \tag{19}$$

where T is the torque applied on the worm, R_w is the base radius of the worm and $\overline{x}_r$ is the transmission error evaluated considering the averaged displacements. Considering the constants in Table 2, the average transmission error is defined in Eq. (20).

$$\overline{x}_r = C_1(\overline{x}_w - \overline{x}_g - R_w\overline{\theta}_w) + C_2(-\overline{y}_w + \overline{y}_g - R_g\overline{\theta}_g) + C_3(\overline{z}_w - \overline{z}_g) \tag{20}$$

It is worth noting that each of the displacements ($\overline{x}_i$, $\overline{y}_i$, $\overline{z}_i$ and $\overline{\theta}_i$) has been considered as the mean value of the displacements of the nodes where the results have been computed in the x-direction, in the y-direction and in the z-direction, respectively. For the

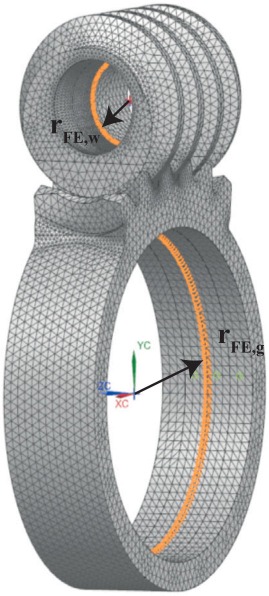

Fig. 6. The radii required for the computation of the averaged displacements for the meshing stiffness evaluation.

Table 3
Geometric parameters.

Parameters	Symbol	Unit	Value
Material of the worm		[–]	C45
Material of the gear		[–]	EN GJL 250
Number of teeth of the worm	Z_w	[–]	1
Number of teeth of the gear	Z_g	[–]	30
Standard module	m	mm	3
Pressure angle	Φ_n	deg	20
Helix angle	λ	deg	5.38
Base radius of the worm	R_w	mm	16
Base radius of the gear	R_g	mm	45.2

sake of clarity, the results have been averaged on the nodes of the radii highlighted in Fig. 6, namely $r_{FE,i}$. As highlighted in [37], the accuracy of the mesh stiffness estimation of full blank spur gears is not affected by the choice of the radius r_{FE}. As this is a new mechanism for this type of FE method, simulations have been conducted at various radii and positions along the axial plane of the body. The results confirm that the choice of radius value and positioning does not affect the resulting meshing stiffness. Therefore, the radii that had been selected are positioned in the transverse planes of the two bodies, along the line that passes through their centers (ref. Fig. 6). It is important to note that the averaged rotational deflection, for both the worm and the gear, are computed using Eq. (21) starting from the mean tangential deflection $\bar{u}_\theta$. The evaluation of these quantities is based on the circumferential reference system of each body, with the origin situated at the center of the bodies.

$$\bar{\theta}_i = \frac{\bar{u}_{\theta_i}}{r_{FE,i}} \tag{21}$$

4. Experimental campaign

This Section is devoted to the description of the system under examination and, consequently, of the experimental campaign that is carried out for the purpose of validating the model. The object of study is a gearbox that contains a right-hand ZI-type worm gear mechanism. The geometrical parameters and materials are delineated in Table 3, which provides comprehensive details on the mechanism. The experimental test bench is illustrated in Fig. 7, which also comprises a detailed scheme to ensure clarity. The control of the test bench is performed through a control panel which allows the determination of both the rotational velocities and the resistant torque on the gear. The worm is connected to an electric motor which causes the worm to rotate. Consequently, the rotation of the worm drives the gear. The resistant torque is controlled by a load device connected to the gear shaft via a coupling mechanism.

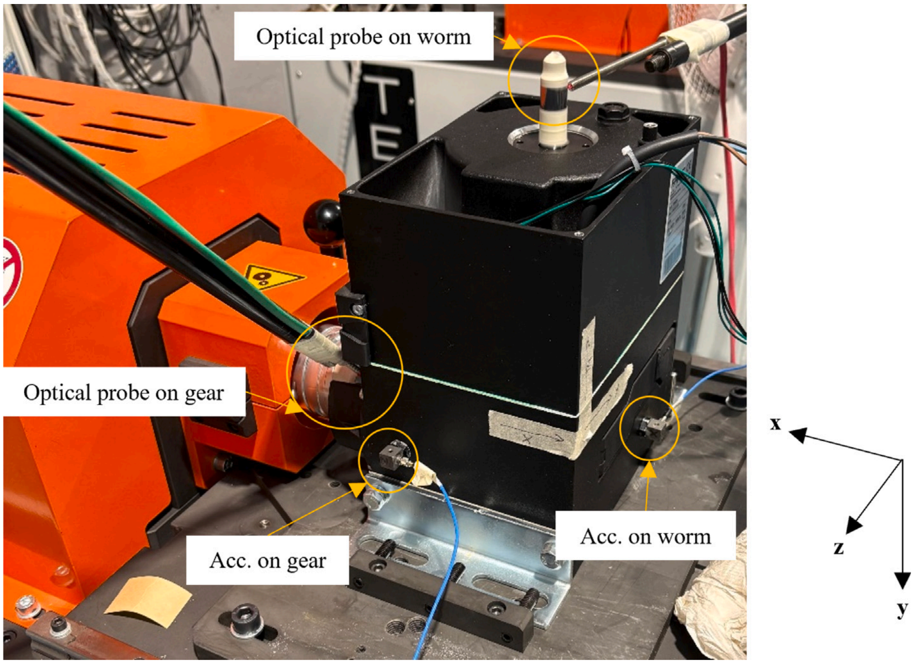

(a) Experimental setup.

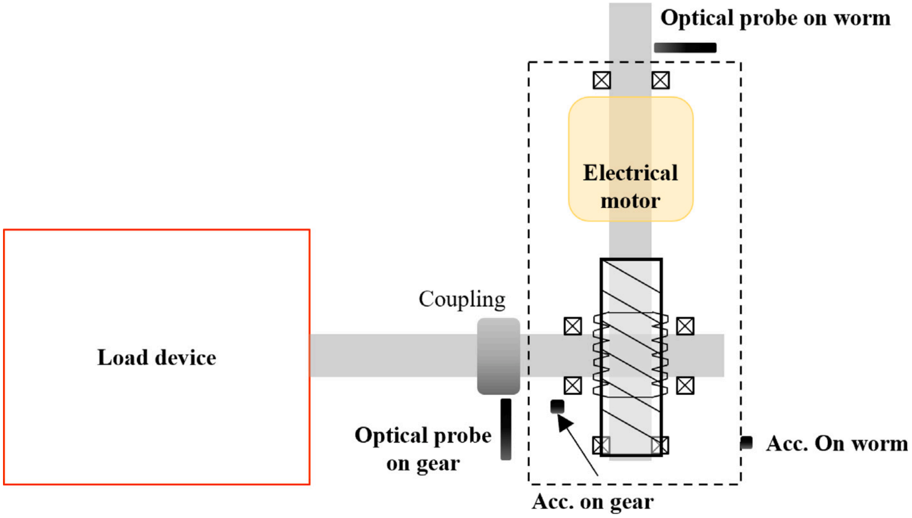

(b) Scheme of the experimental setup.

Fig. 7. Experimental setup.

In order to measure the quantities related to the rotational DOFs, two optical probes are placed on the shafts of the gear and the worm. As illustrated in Fig. 7, the optical probes act on the zebra tapes which are attached to the shafts. The number of output pulses per revolution, deriving from the zebra tapes, is 25 for the worm and 215 for the gear. From these quantities, it is possible to derive the number of output pulses per second directly, which allows for calculating the rotational speeds. The angular displacements are then calculated by integrating the velocities. It should be noted that the measurement of the torsional oscillations of the two shafts plays a crucial role in the assessment of the model validation, as it allows for a direct correlation between the experimental and the numerical data. As a matter of fact, starting from these quantities, it is possible to derive the transmission error of the two mating gears which accurately describes the dynamic behavior of the system. Notwithstanding, the experimental procedure for obtaining torsional oscillations is inherently challenging due to the number of ppr required to generate a signal with a satisfactory frequency field. Notably, the frequency range is directly influenced by the number of ppr and the rotational frequency of the shafts. The choice of tape resolution is thus crucial.

Table 4
Speed and resistant torque of the experimental tests.

Parameters	Symbol	Unit	Values		
Worm velocity	$\dot{\theta}_w$	(rpm)	1200	1800	2100
External torque on the gear	$T_{e,g}$	(N m)	4	8	12

Table 5
Torque values for the numerical meshing stiffness estimation.

Torque (N m)						
0.5	2	5	8	12	15	20

Table 6
Value of the radii required for the computation of the averaged displacements for the meshing stiffness evaluation.

Parameters	Unit	Value
$r_{FE,w}$	(m)	1.0e−4
$r_{FE,g}$	(m)	3.5e−4

In addition to the instrumentations previously referenced, two accelerometers (model PCB 356B21) are mounted on the gearbox housing, in close proximity to the bearing housing locations. For the sake of clarity, these accelerometers are referred to as $Acc.worm$ and $Acc.gear$ whose positions are shown in Fig. 7. The selection of these locations is contingent upon the necessity to achieve a measurement that is closely aligned with the bearing forces obtained by the LP model. The acquisition parameters are defined by a sampling frequency of 25 600 Hz and a frequency resolution of 1 Hz.

Within this experimental setup, a series of tests are conducted, in which the speed and the resistant torque applied to the gear are varied. The respective values are presented in Table 4 for reference. The present series of experiments facilitates the investigation of the impact of the velocity and the torque on the system quantities. It should be noted that the range of operating conditions is chosen based on the allowable range for this mechanism. However, it is interesting to underline that the resistance torque has tripled from 4 N to 12 N.

5. Model results and parametric analysis

This section presents the findings derived from the implementation of the numerical models. Initially, the meshing stiffness results are investigated. The outcomes of the validation procedure are then presented, encompassing a comparison between the experimental and numerical results. Consequently, a sensitivity analysis is conducted on pivotal parameters of the model.

5.1. Meshing stiffness results

In accordance with the protocol outlined in Section 3, the meshing stiffness results are obtained for twelve simulated positions of the gears, from 0% to 100% of the angular pitch and for different resistant torques, the values of which are documented in Table 5. It is important to emphasize that the outcomes of the FE model are derived from the radii enumerated in Table 6, with reference to Fig. 6. It should be noted that, in the case of spur gear mechanisms, the mean transmission errors are calculated based solely on the rotational degrees of freedom. Whereas, for worm gear mechanisms, translational DOFs have been considered in addition to rotational ones. In order to verify this assumption, Fig. 8 presents an example of the averaged contributions multiplied by the director cosines as shown in the definition of transmission errors in Eq. (20). The results of this analysis pertain to the simulation of the system at 0% of the angular pitch, in conjunction with a resistant torque of 8 N m. Similar results can be achieved by examining alternative gear positions and different torques. As shown in Fig. 8, the main contributions are related to the rotation of the worm, while the contributions of the translation in the y-direction and the rotation of the gear are also significant. As a consequence, it has been chosen to consider all the contributes in the definition of the meshing stiffness.

In order to gain a deeper insight into the trend of the meshing stiffness, the computed Von Mises stress has been plotted for three angular positions (0%, 33% and 58%) in relation to the simulations with 8 N m of applied torque. First, it is worth noting, from the analysis of Figs. 9 and 10, that the path of the contact is in agreement with the ones found in the literature [24,25,40]. At the beginning of tooth contact, which occurs at 0% of the angular pitch, two teeth are in contact. As the angular pitch reaches 33%, the third tooth comes into contact. Localized stress concentrations are observed, as commonly observed in this class of gear mechanisms [24]. Although mesh refinement could reduce these peaks, their effect on meshing stiffness is negligible, as stiffness is primarily influenced by global displacement rather than local stress values.

Therefore, the results of the FE method are presented in Fig. 11, where the meshing stiffness values are plotted against the percentage of angular pitch for each applied torque. It should be noted that, as would be expected, for each simulated positioning of the gears, the meshing stiffness values increase as the torque increases. It is important to note that the developed dynamic model enables the selection of the meshing stiffness value based on the instantaneous transmission error and the percentage of the angular

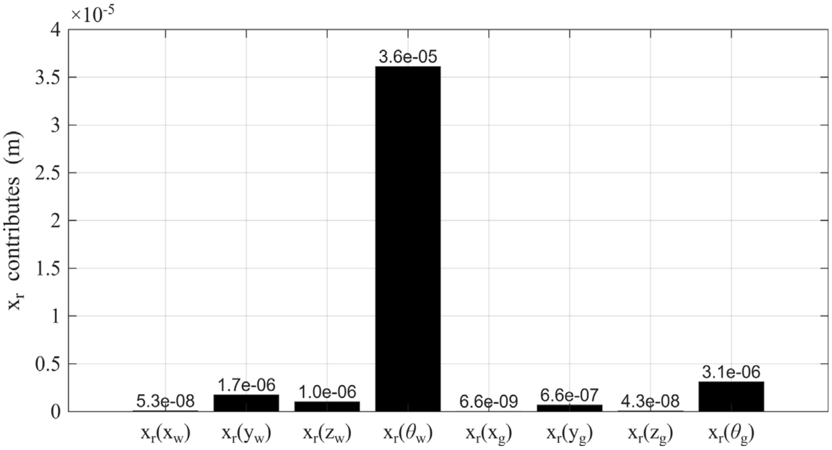

Fig. 8. Transmission error contributes related to each considered DOF.

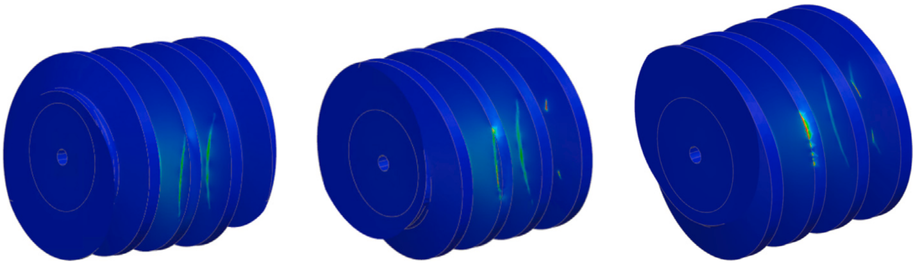

(a) 0% of the percentage on the angular pitch.

(b) 33% of the percentage on the angular pitch.

(c) 58% of the percentage on the angular pitch.

Fig. 9. Von Mises stress on worm body.

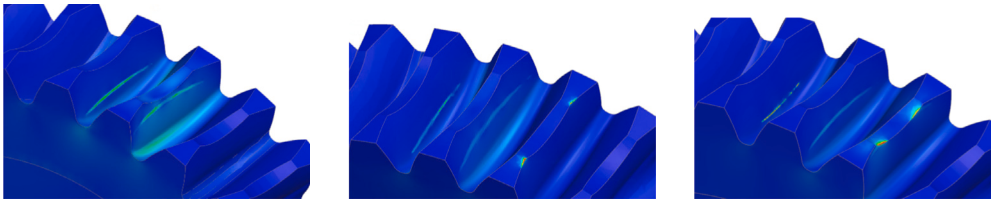

(a) 0% of the percentage on the angular pitch.

(b) 33% of the percentage on the angular pitch.

(c) 58% of the percentage on the angular pitch.

Fig. 10. Von Mises stress on gear body.

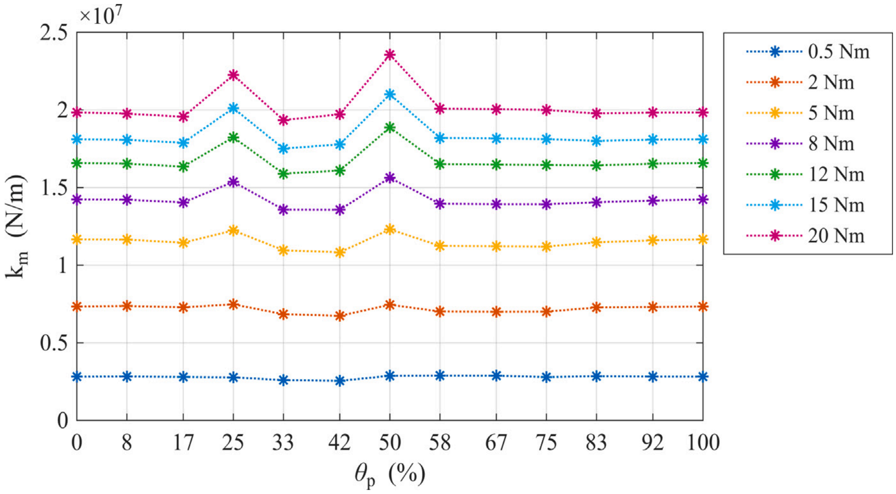

Fig. 11. Meshing stiffness results at various angular positions and resistant torques.

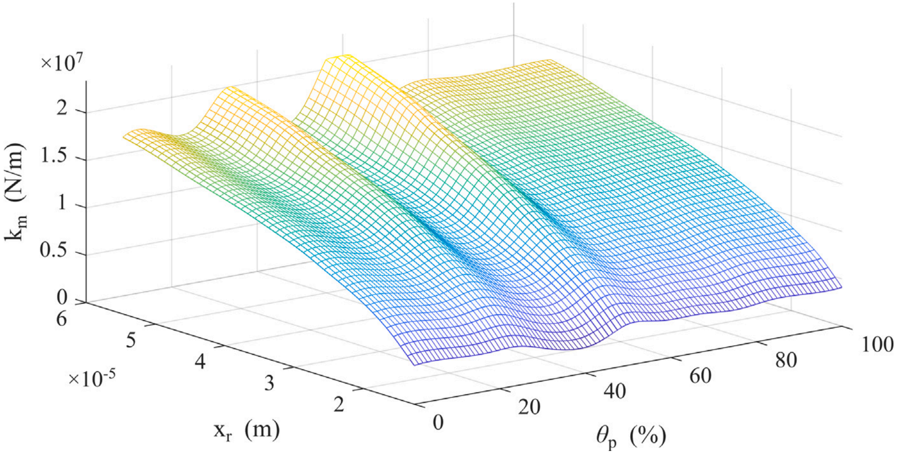

Fig. 12. Meshing stiffness surface.

pitch. For this reason, the obtained meshing stiffness is expressed as a function of the transmission error rather than the torque. Moreover, a resampling of the meshing stiffness depending on the refinement of the transmission error values and a refinement of the angular positioning is performed. The results are shown in Fig. 12. Although minor changes in amplitude are observed with varying torque levels, the overall waveform profile remains consistent across all operating conditions. This is primarily due to the system behaving as a quasi-rigid body within the tested range, where resonance effects are negligible. Furthermore, the torque values applied in this study are relatively low compared to those typically seen in other gear systems, which contributes to the limited variation in dynamic response.

5.2. LP model results

The numerical simulations are performed in the AMESim environment using the fixed-time step integrator based on the fourth-order Runge–Kutta method. A time step of 1e−5 s is used throughout the study. Table 7 details the input parameters of the LP model. The damping coefficients (α and β) are selected to achieve a damping factor ζ of 2% to 10% within the frequency range of interest. The typical operational condition of the machine under study is used as a reference point. The simulations are conducted according to the experimental operational parameters delineated in Table 4.

5.2.1. Validation protocol

In the context of validating the model, the employed signal processing is outlined hereinafter. The scope is verifying the capacity of the model to accurately represent the actual behavior of the mechanism. It is important to note that the following signal processing

Table 7
Parameters of the lumped parameter model.

Parameters	Symbol	Unit	Value
Friction coefficient	μ	[−]	0.05
Rayleigh's damping mass proportionality coefficient	α	(1/s)	1
Rayleigh's damping stiffness proportionality coefficient	β	(s)	5e−4
Bearing stiffness	k_b	(N/m)	1e+8
Input shaft torsional stiffness	k_t	(N m/rad)	5.5e+5

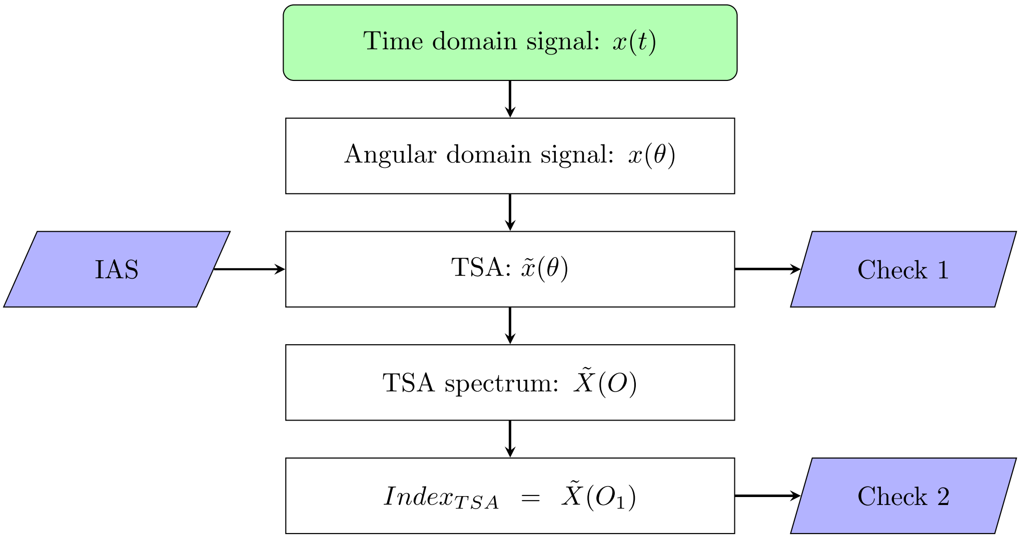

Fig. 13. Flowchart for the signal processing.

is performed for both the experimental and numerical outcomes. The flowchart in Fig. 13 illustrates the signal processing employed for the model validation.

The process under consideration begins with a generic signal in the time domain. This is then subjected to interpolation to pass from the time domain to the angular domain. Consequently, the angular average was performed by employing the instantaneous angular speed (IAS) of the worm (Ref. [41]). The rotational frequency of the worm is selected based on the fact that it also represents the meshing frequency of the mechanisms. This kind of average facilitates the elimination of all components that do not align with the rotational dynamics of the worm. This property is particularly advantageous in the context of experimental signal analysis, given that such signals are characterized by the presence of undesirable noise components, such as those originating from the electrical engine. The synchronous average in the angle domain is first employed as a comparison, namely Check 1, between the experimental and the numerical results, providing information about the shape of the signals. Therefore, the spectrum of the synchronous average in the order domain is performed with the objective of investigating the amplitude of the meshing components, since each order corresponds to the meshing frequency. In the present study, it was decided to make a comparison exclusively of the first harmonic of the meshing order, namely $Index_{TSA}$, in order to enhance clarity. It is assumed that this quantity is representative of the dynamic behavior of the system.

5.2.2. Validation results

The present section is dedicated to the investigation of the experimental and the numerical results, with the objective of evaluating the influence of the velocity and the resistant torque on the worm gear dynamics. In order to validate the model, two types of comparisons are performed. At first, the experimental accelerations are compared with the numerical bearing forces. The decision is reached on the assumption that the frequency response function is flat and does not show resonances in the frequency range of interest. Indeed, the measurement points were chosen in close proximity to the bearing housing location, i.e. the position of application of the bearing forces. In these locations, it is considered that the case has a high stiffness. Consequently, the data will be normalized to facilitate improved understanding, since the model enables the calculation of the bearing forces, instead of the accelerations of the gearbox case, which were measured during the experimental campaign.

Second, as a key point of the model validation, the transmission errors are studied. This comparison is of paramount importance, as it facilitates the evaluation of analogous quantities. In addition, the choice of this quantity for comparison avoids the influence of the gearbox housing. It is important to acknowledge that the transmission errors are calculated with reference to the rotational DOFs only, specifically θ_w and θ_g, as indicated in Eq. (22). The decision to consider solely the rotational DOFs is predicated on the

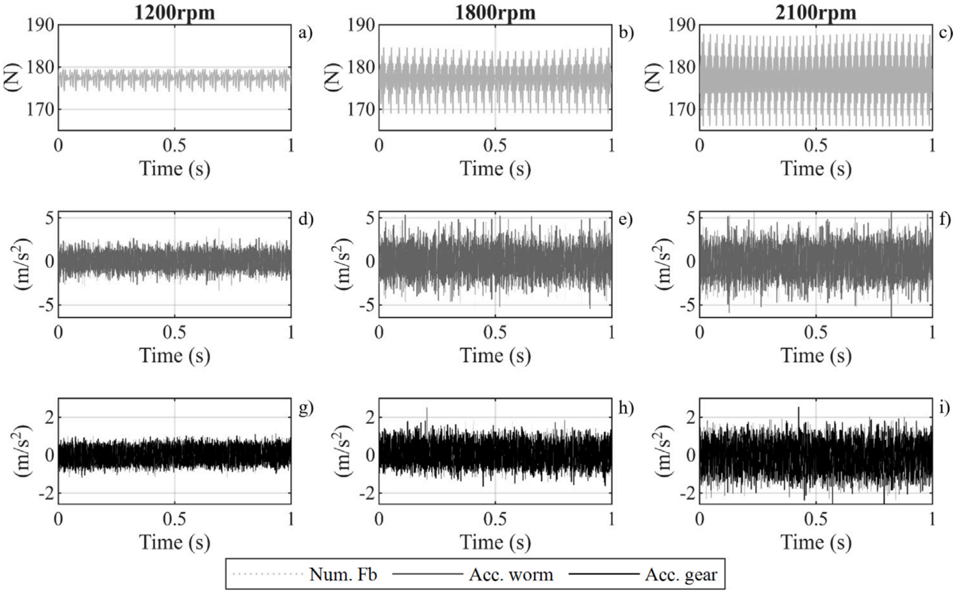

Fig. 14. Time domain signals of the test with 8 N m of resistant torque considering the y-direction.

fact that the experimental campaign allows for the acquisition of these quantities only.

$$x_r(t) = cos\Phi_n sin\lambda R_w \theta_w(t) - cos\Phi_n cos\lambda R_g \theta_g(t) \tag{22}$$

The influence of the velocity is investigated through an analysis of the trend of the investigated quantities, considering two different resistant torques: 8 N m and 12 N m. For clarity, the time signals for the input in the procedure are shown in Fig. 14, which contains the numerical bearing forces and the experimental accelerations of both accelerometers, namely $Acc.worm$ and $Acc.gear$, in the y-direction and considering the tests at 8 N m of resistant torque. It should be noted that the time-domain waveforms of the numerical and experimental signals differ. This is because the experimental accelerations contain background noise, which is not modeled in the developed LP model. As a consequence, the comparisons are performed following Check 2, described in the flowchart in Fig. 13, which involves the calculation of the $Index_{TSA}$. This particular signal processing method makes it easier to investigate only the fluctuation of the dynamic components of interest. It is noteworthy, from the time domain signals, that the fluctuation amplitudes increase in proportion to the velocity. Furthermore, as demonstrated in Fig. 14, the mean value of the bearing forces remains constant. The results of the $Index_{TSA}$, considering all the directions, are shown in Figs. 15 and 16. The numerical outcomes demonstrate a rising trend following the increase in rotational speed. The acceleration results of all the accelerometers exhibit a comparable trend that is correlated with the numerical outputs. It is also observed that the higher values of the $Index_{TSA}$ are in the y-directions, as evidenced by both the numerical and the experimental results. In order to further investigate the matter, a comparative analysis of the data is conducted. This involves merging the data into a single graph and its normalization. It is worth clarifying that the data are normalized considering the maximum value of each graph separately. For instance, with regard to Fig. 15(a), the data are subjected to normalization by dividing all the values obtained for the velocities under consideration (1200, 1800 and 2100 rpm) by their maximum value, which is the value of the test at 2100 rpm. This representation facilitates a more precise evaluation of the velocity influence and a direct comparison between different quantities. Fig. 17 shows the normalized data of the test at 8 N m of resistant torque. Although Fig. 18 provides a visual representation of the results obtained from the tests at 12 N m. The analysis of the results confirmed that the amplitudes of the first meshing order increase with the velocity, passing from 1200 rpm to 2100 rpm. In all directions, the trends are highly analogous. It is noteworthy that the experimental findings generally demonstrate a more pronounced increase in amplitude with increasing velocity compared to the numerical data. The aforementioned disparities are more pronounced in the x-direction. Nonetheless, the developed model is able to capture the overall trend observed in the experimental acceleration data, confirming its effectiveness in reproducing the main dynamic characteristics of the system.

Analogous data processing is used to examine the impact of different resistant torques. Within this scope, the following graphs investigate the tests at 1200 rpm of rotational velocity as a representative example of the operating conditions for which the gearbox is designed. As illustrated in Fig. 19, the initial data of the procedure comprises the numerical bearing forces and the experimental accelerations. For the sake of brevity, only the y-direction is displayed. It is important to note that the mean values of the bearing forces demonstrate a variation at distinct torques. In particular, the average values increase as the torque increases. However, when the results of the tests with a constant torque are considered (see Fig. 14), the mean values remain constant. Consequently, to investigate the influence of the torque, the $Index_{TSA}$ of the bearing forces and the experimental accelerations is displayed in Fig. 20. The numerical outputs indicate a slightly ascending trend of the meshing components across the various torques. The results in the y-directions demonstrate the higher values of the meshing components, both for the numerical and experimental results. It

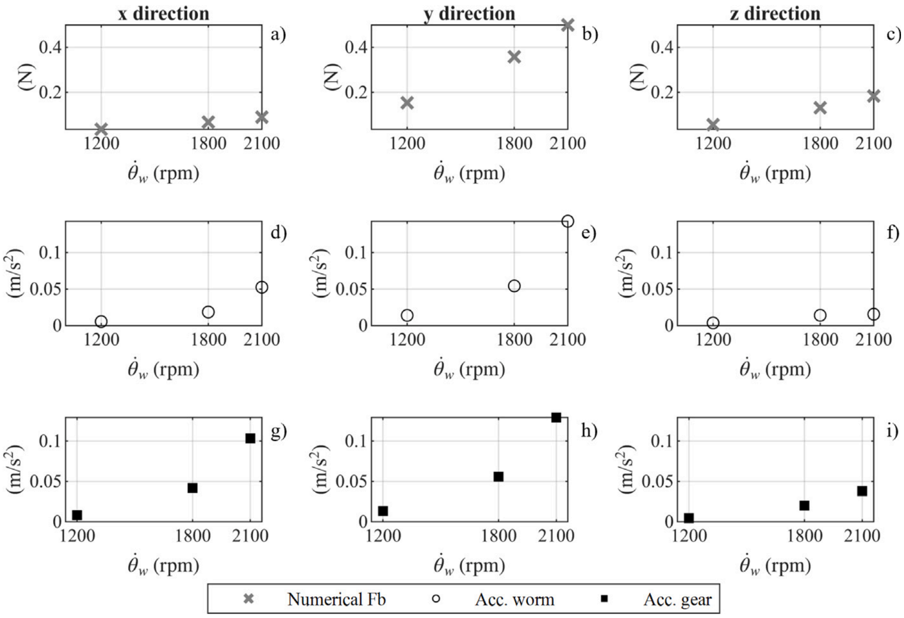

Fig. 15. Comparison between the $Index_{TSA}$ values of the numerical bearing forces and the experimental acceleration of the tests with 8 N m of resistant torque.

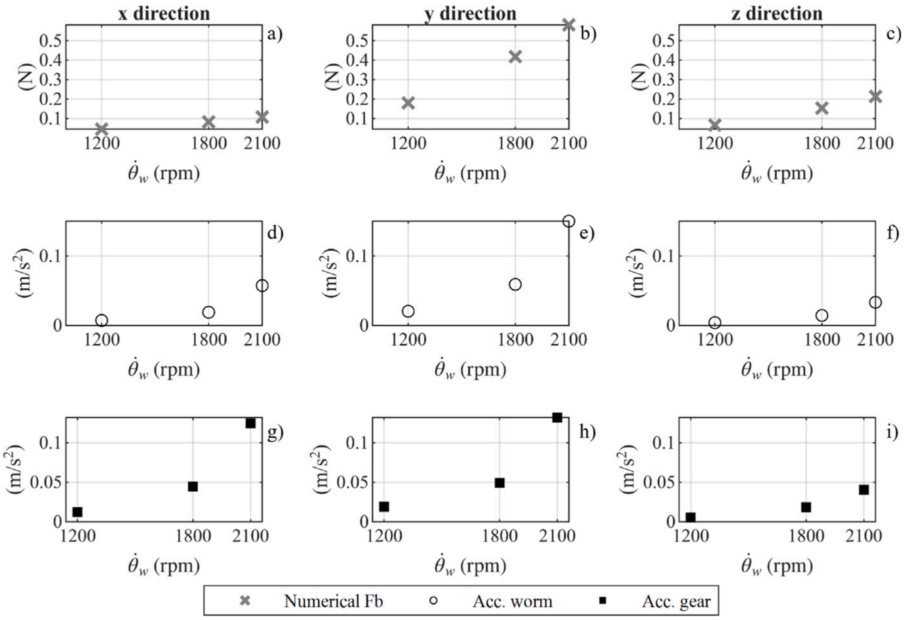

Fig. 16. Comparison between the $Index_{TSA}$ values of numerical bearing forces and the experimental acceleration of the tests with 12 N m of resistant torque.

is noteworthy that the $Index_{TSA}$ remains almost constant with the change in the resistant torque, especially when the z-direction is considered. This outcome is confirmed by the normalized results in Fig. 21, which show the comparison between the numerical outputs and the results of the accelerometer on the worm. The normalization procedure is consistent with the methodology employed in the analysis of the tests conducted at varying velocities. Focusing on Fig. 21, it can be assumed that the LP model can detect the influence of different resistant torques. Fig. 22 presents the results obtained from the tests conducted at a worm rotational speed of 1800 rpm. The numerical outcomes exhibit a slightly increasing trend across all considered directions (x, y, and z). Although the variation in the index values remains minimal, especially if compared with the results at different velocities in Figs. 17 and 18. In contrast, the experimental data reveal a different behavior: in both the x- and y-directions, a slightly decreasing trend is observed,

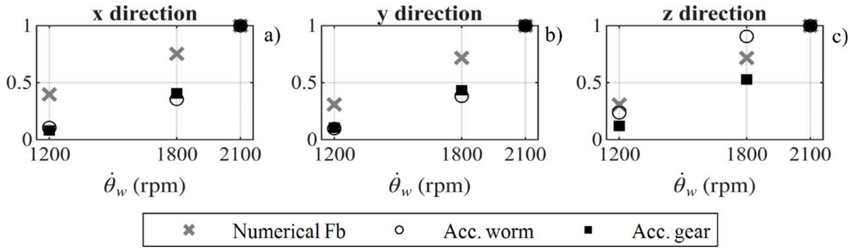

Fig. 17. Comparison between the normalized amplitudes of the synchronous average first order of the numerical bearing forces and the experimental acceleration of the tests with 8 N m of resistant torque.

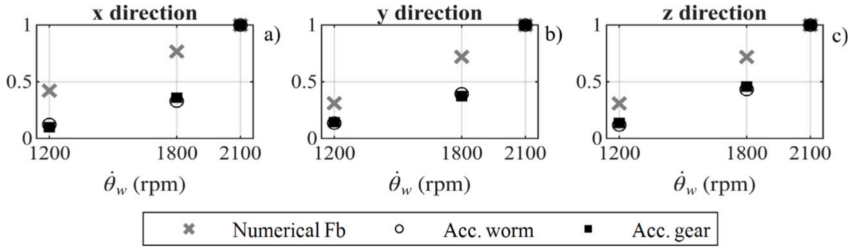

Fig. 18. Comparison between the normalized amplitudes of the synchronous average first order of the numerical bearing forces and the experimental acceleration of the tests with 12 N m of resistant torque.

suggesting a modest attenuation in the dynamic response. For the z-direction, the experimental trend remains essentially stable, with negligible variations in the index value. This comparison highlights a partial divergence between the numerical and experimental results at this specific speed. The numerical results confirm the expected behavior and are consistent with those obtained at 1200 rpm. The trend observed in the experimental data is likely influenced by background noise, which may obscure the effect of the resistant torque, as the variations between different torque levels are relatively small.

The experimental and the numerical transmission errors are thus compared. It is worth noting that the transmission error data are normalized for confidential reasons. The comparisons are made considering the synchronous average of the signals in the angular domain, namely Check 1 in the flowchart in 13. Within these comparisons, the shape of the signals must be investigated within a complete rotation of the shafts (from 0 to 360 degrees). The results are displayed in Fig. 23, which illustrates the transmission errors of the tests with 4, 8 and 12 N m of resistant torque at three different rotational velocities: 1200 rpm, 1800 rpm and 2100 rpm. The solid black line represents the transmission error computed starting from the experimental data, while the gray dotted line refers to the transmission error computed from the LP model outputs. It is worth noting that the shape of the numerical and the experimental transmission error is very similar, considering all the tests at 1200 rpm and 1800 rpm. Despite sufficient motor and brake sizing for operation at 2100 rpm, the controller exhibited limited capability to regulate speed fluctuations at high speeds. As the model assumes a constant input speed for the electric motor, this resulted in larger discrepancies between experimental and numerical results for operations at 2100 rpm under low torque conditions (4 N m).

5.3. *Sensitivity analysis*

As mentioned in Section 1, the majority of the available worm gear lumped parameter models take into account the damping of the system by adopting the Rayleigh damping model [11] or by incorporating the friction coefficient as a component of the dynamic equation [17,18]. It was determined that further investigation was necessary to ascertain the influence of differing contributions on the dynamics of the worm gear. To this end, an analysis of the contributions of the model equations is conducted, with a comparison being made on the proportional viscous damping, the meshing and the friction forces resulting from the simulation. For the sake of clarity, the equation contributions are summarized in Table 8.

As a result of the model simulation, Fig. 24 depicts the time domain output forces of the LP model in the x, y, and z-directions, considering 1800 rpm of rotational velocity. The meshing forces are displayed in Fig. 24a, b and c, the viscous forces in Fig. 24d, e and f, and the friction forces in Fig. 24g, h. In fact, as mentioned in Section 2, the friction forces have no components in the

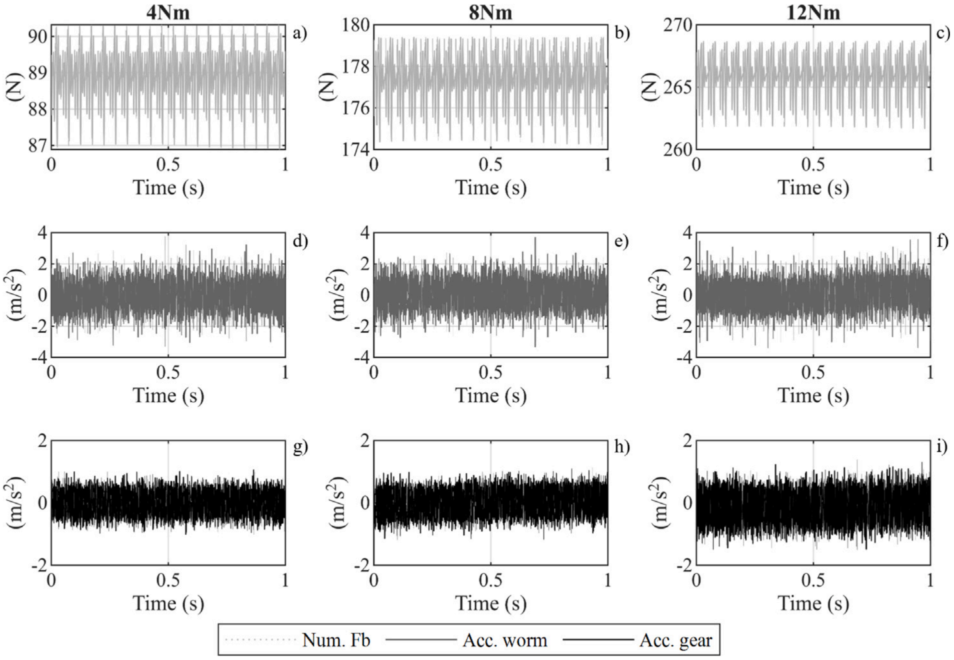

Fig. 19. Time domain signals in the y-direction of the test with 1200 rpm of velocity.

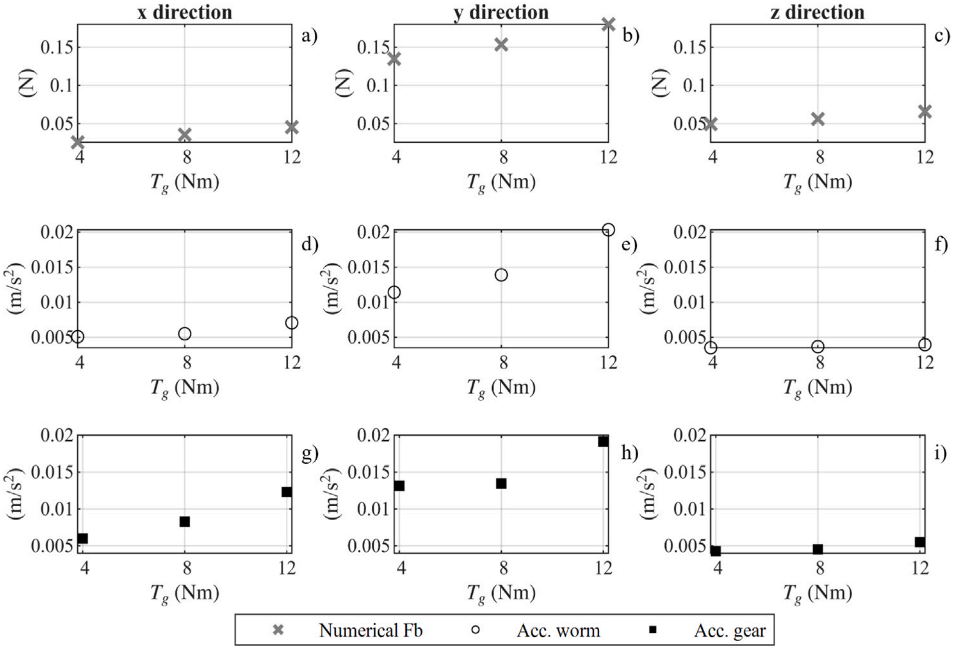

Fig. 20. Comparison between the $Index_{TSA}$ values of the numerical bearing forces and the experimental acceleration of the tests at 1200 rpm of the worm velocity.

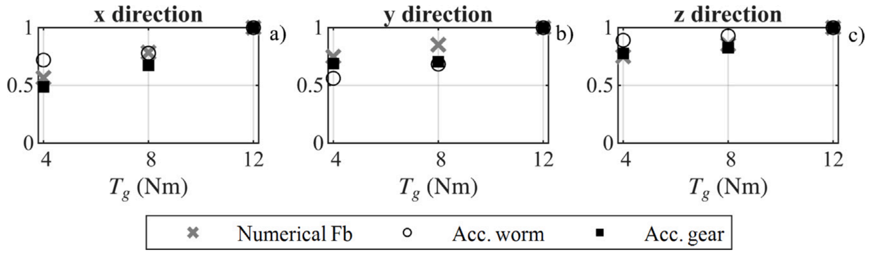

Fig. 21. Comparison between the normalized amplitudes of the synchronous average first order of the numerical bearing forces and the experimental acceleration of the tests at 1200 rpm of the worm velocity.

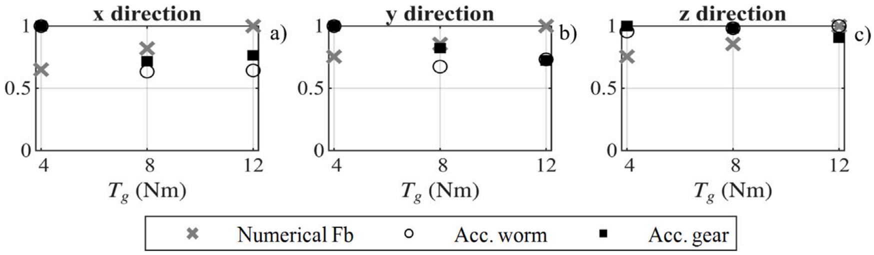

Fig. 22. Comparison between the normalized amplitudes of the synchronous average first order of the numerical bearing forces and the experimental acceleration of the tests at 1800 rpm of the worm velocity.

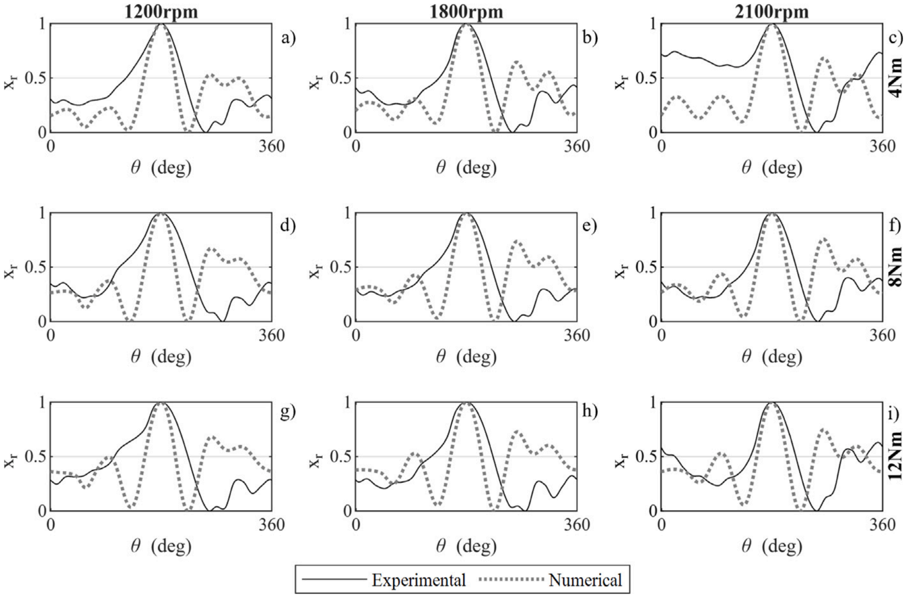

Fig. 23. Comparison between the numerical transmission errors and the experimental transmission errors in the angular domain.

z-direction. As demonstrated in Fig. 25, the frequency components of the forces are illustrated, including the meshing component (equal to 30 Hz in these specific simulations) and its harmonic. It is noteworthy that all of the considered forces exhibit the same frequency components.

In order to investigate the influence of the various components on the system dynamics, a comparison is made considering both the average values of the forces and the dynamic components. The mean values of the forces are outlined in Fig. 26. Firstly, it is important to note that a correlation exists between higher energy contributions and meshing. Furthermore, it is observed that the higher values of the meshing and the damping components are located in the y-direction. While, when considering the friction

Table 8
Details on the equation contributions.

Component	Equations contribution
Meshing	$\mathbf{K}\mathbf{q}$
Viscous	$\alpha\mathbf{M}\dot{\mathbf{q}} + \beta\mathbf{K}\dot{\mathbf{q}}$
Friction	$\mathbf{K}_f\mathbf{q}$

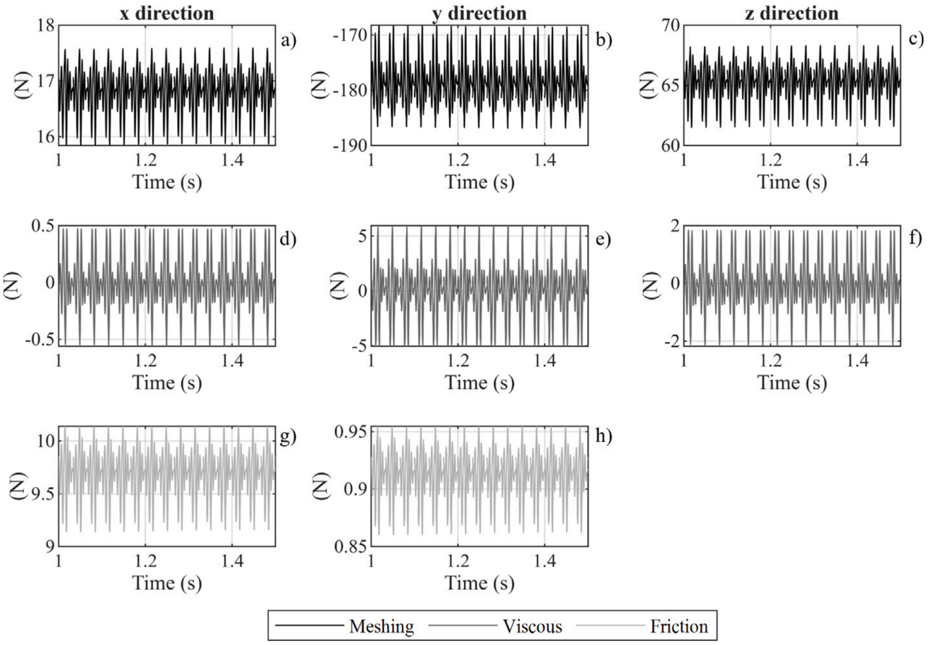

Fig. 24. Output forces of the LP model in the time domain, including detailed contributions from meshing, viscous, and friction forces.

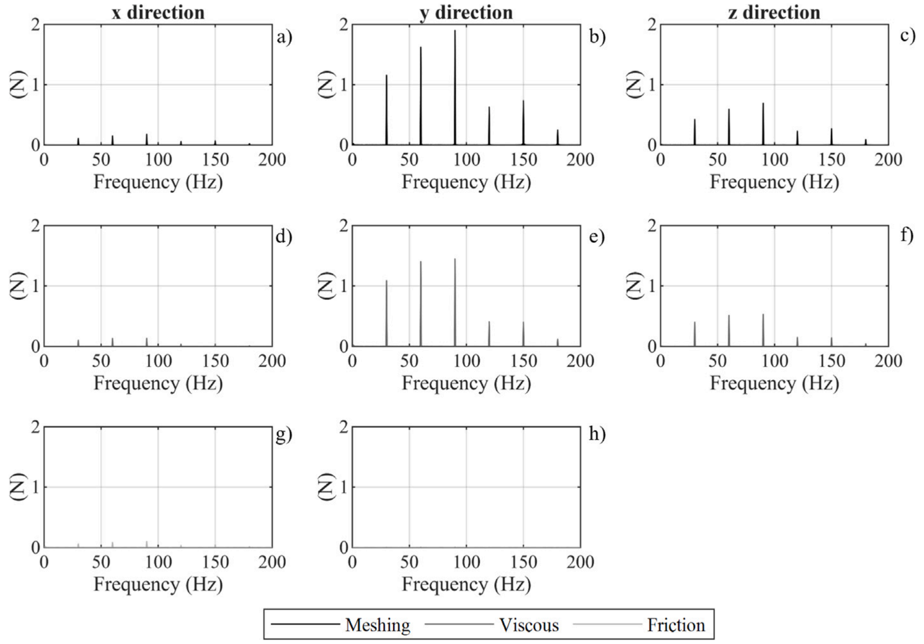

Fig. 25. Output forces of the LP model in the frequency domain, including detailed contributions from meshing, viscous, and friction forces.

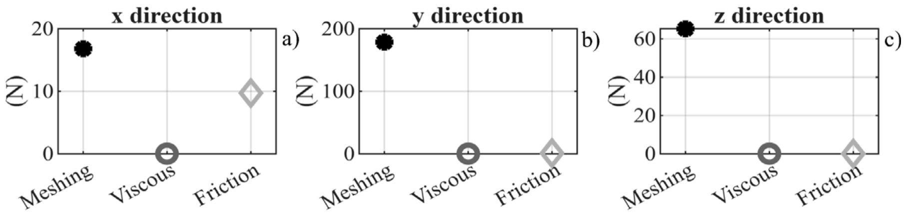

Fig. 26. Average values of the output forces of the LP model, including detailed contributions from meshing, viscous, and friction forces.

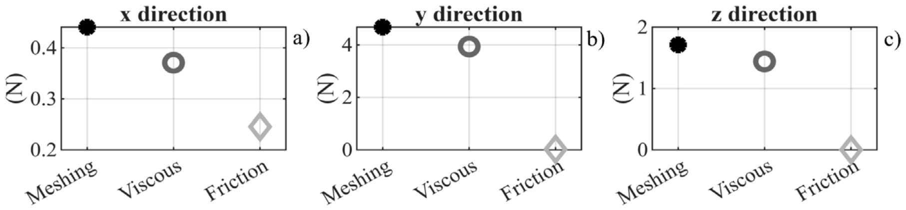

Fig. 27. Sum of the first three meshing harmonics of the output forces of the LP model, including detailed contributions from meshing, viscous, and friction forces.

Table 9
Friction coefficient values.

Parameter	Values				
μ [−]	0	0.02	0.05	0.07	0.1

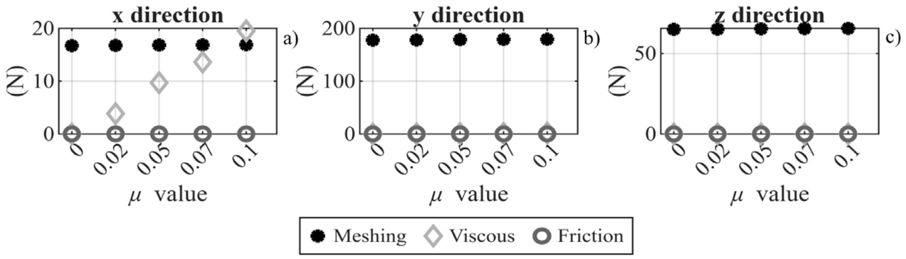

Fig. 28. Average values of the output forces of the LP model. Comparison between the results with different friction coefficient values.

components, it is evident that the higher values are noted in the x-direction. Therefore, it should be noted that, as illustrated in Fig. 26a, the average value of the friction component is comparable to the meshing value. As a consequence, it is evident that the friction components play a crucial role in the system and they must not be neglected. As a further investigation, the dynamic components are investigated in Fig. 27. The plotted values refer to the sum of the first three meshing components of the spectra. It is interesting to note that the dynamic components of the viscous and the meshing forces are analogous. Thus, it is mandatory to also take into account the components related to the damping when modeling the worm gear mechanisms. Moreover, it is noticed that, in the x-direction, the friction dynamic components are not negligible. These results confirm the importance of modeling both the contributions related to the damping and the friction.

In order to further investigate the dynamics of the worm gear, a parametric analysis is performed in order to ascertain the role of the friction components in such dynamics. As mentioned in the previous sections, friction contribution is of great importance in these types of mechanisms. Therefore, a deeper understanding is necessary to investigate how it affects the model outputs. Table 9 lists the investigated friction coefficients, whose values are chosen based on the literature review [13,15,18]. For each of the aforementioned friction coefficients, a numerical simulation is conducted with the objective of understanding the effect of these coefficients on the model outcomes. The comparisons that were performed concerned the mean values of the forces, as illustrated in Fig. 28. It should be noted that only the forces in the x-direction are sensitive to the change in the friction coefficient value. In addition, a study of the data reveals that when the friction coefficient is set at 0.07 or 0.1, the mean values of the friction forces are in accordance with the mean values of the meshing forces in the x-direction (ref. Fig. 28a). Analogous considerations may be applied when assessing the sum of the first three meshing harmonics, whose results are displayed in Fig. 29.

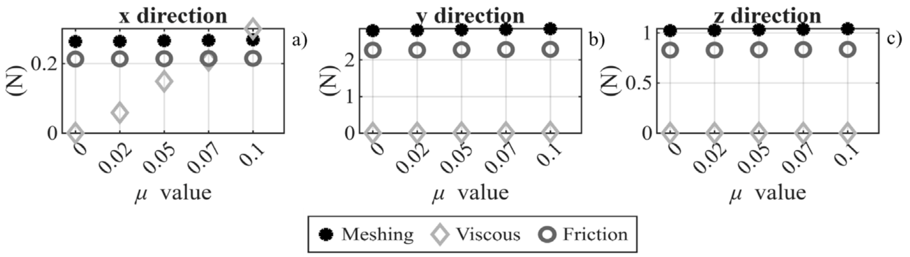

Fig. 29. Sum of the first three meshing harmonics of the output forces of the LP model. Comparison between the results with different friction coefficient values.

6. Summarizing remarks

The dynamic model of a worm gear mechanism was developed starting from the equation writing. The model comprises components related to friction phenomena and a numerically assessed load-dependent time-varying meshing stiffness. In addition, the utilization of coefficients, designated as C_H and C_R, facilitates the resolution of both left- and right-hand mechanisms, in addition to the CW and CCW rotations. To enhance understanding of worm gear dynamics, a numerical meshing stiffness surface was obtained using a pure FE method. Specifically, the averaged slope approach proposed by Cooley was used to estimate the meshing stiffness of spur gears. The methodology to obtain the meshing stiffness was exploited, detailing the FE model components and the quantities which contribute to the meshing stiffness definition. The reliability of the findings was validated through a numerical comparison with the contact area values reported in the existing literature.

An experimental campaign was conducted with the objective of validating the model. The experimental setup is detailed, including a comprehensive account of the instrumentation utilized. Consequently, a wide range of operational conditions was investigated, thereby facilitating the acquisition of the acceleration data and the transmission errors. The experimental and numerical results were compared on the basis of the angular domain signal analysis, a technique that facilitates the investigation of dynamic components of interest. The translational DOFs were first analyzed, revealing that dynamic components of both numerical bearing forces and experimental accelerations increase with velocity. In all cases, the y-direction exhibited the highest dynamic response. While torque had minimal effect on the x- and z-directions, it led to an increase in dynamics along the y-direction. Rotational DOFs were then compared, incorporating transmission errors. The TSA of numerical and experimental results showed analogous patterns. In conclusion, a comparison of the numerical and experimental results confirms the capability of the developed LP model to capture the influence of both the change in velocity and the resistant torque. Additionally, the model exhibits the capacity to replicate the shape and magnitude of the transmission error across a range of torques and velocities.

In order to enhance understanding of the LP model, a detailed analysis of its equation components was performed, with particular emphasis on proportional viscous damping and friction, as most existing models incorporate only one of these terms. The outcomes revealed that it was crucial to take into account both the contributions of friction and proportional viscous damping. The friction components have been found to exhibit a higher influence in the x-direction. This phenomenon persisted until a value of the friction coefficient of 0.1 was attained, at which threshold the friction components exceeded those of the meshing components.

CRediT authorship contribution statement

Giulia Cristofori: Writing – review & editing, Writing – original draft, Validation, Software, Methodology, Investigation, Formal analysis, Data curation, Conceptualization. **Mattia Battarra:** Writing – review & editing, Visualization, Supervision, Methodology, Data curation. **Emiliano Mucchi:** Supervision, Project administration.

Declaration of competing interest

The authors declare that they have no known competing financial interests or personal relationships that could have appeared to influence the work reported in this paper.

Acknowledgments

The authors thank the technicians of FAAC Industries for providing the experimental apparatus and for their assistance during the experimental campaign.

Data availability

The data that has been used is confidential.

References

[1] E. Mucchi, A. Rivola, G. Dalpiaz, Modelling dynamic behaviour and noise generation in gear pumps: Procedure and validation, Appl. Acoust. 77 (2014) 99–111.
[2] F. Pizzolante, M. Battarra, G. D'Elia, E. Mucchi, A rattle index formulation for single and multiple branch geartrains, Mech. Mach. Theory 158 (2021) 104246.
[3] B. Mooring, D. May, M. Schulte, Modeling and analysis of a manipulator joint driven through a worm gear transmission, J. Mech. Des. 112 (4) (1990) 551–556.
[4] D. May, S. Jayasuriya, B. Mooring, Modeling and control of a manipulator joint driven through a worm gear transmission, J. Vib. Control 6 (1) (2000) 85–111.
[5] M. Chung, D. Shaw, Parametric study of dynamics of worm and worm-gear set under suddenly applied rotating angle, J. Sound Vib. 304 (1–2) (2007) 246–262.
[6] W.R. Brown, A.G. Ulsoy, A passive-assist design approach for improved reliability and efficiency of robot arms, in: 2011 IEEE International Conference on Robotics and Automation, IEEE, 2011, pp. 4927–4934.
[7] C.l. Bordegaray, G. Ferraris, M. Guingand, J.-P. de Vaujany, Dynamic behavior simulation of a worm gear, in: International Design Engineering Technical Conferences and Computers and Information in Engineering Conference, Vol. 4742, 2005, pp. 883–890.
[8] Y. Benabid, S. Mansouri, Dynamics study and diagnostics with vibration analysis from worm gear manufactured by reverse engineering techniques, J. Vibroengineering 18 (7) (2016) 4458–4471.
[9] A.E. Chakroun, A. Hammami, A. De-Juan, F. Chaari, A. Fernandez, F. Viadero, M. Haddar, Modal energetic analysis and dynamic response of worm gear drives with a new developed dynamic model, C. R. Méc. 349 (2) (2021) 241–258.
[10] C. Hammami, A.E. Chakroun, A. Hammami, F. Chaari, A. De-Juan, A. Fernandez, F. Viadero, M. Haddar, New approach to study the dynamic performance of worm gear drive model, J. Vib. Eng. Technol. 11 (4) (2023) 1407–1415.
[11] A.E. Chakroun, A. Hammami, C. Hammami, A. de Juan, F. Chaari, A. Fernandez, F. Viadero, M. Haddar, Numerical and experimental study of the dynamic behaviour of a polymer-metal worm drive, Mech. Syst. Signal Process. 193 (2023) 110263.
[12] F. Liu, Y. Chen, B. Lu, W. Luo, B. Chen, Study on the vibration characteristics of worm helical gear drive, Mech. Mach. Theory 191 (2024) 105484.
[13] M.C. Shin, S.H. Kim, G.H. Cho, C.N. Chu, Development of a steering-system model considering viscous friction and its verification, Proc. Inst. Mech. Eng. Part D: J. Automob. Eng. 228 (2) (2014) 144–163.
[14] S.H. Kim, M.C. Shin, J.W. Byun, K.H. O, C.N. Chu, Efficiency prediction of worm gear with plastic worm wheel, Int. J. Precis. Eng. Manuf. 13 (2012) 167–174.
[15] E. Garcia, P. Gonzalez de Santos, C. Canudas de Wit, Velocity dependence in the cyclic friction arising with gears, Int. J. Robot. Res. 21 (9) (2002) 761–771.
[16] Y. Li, T. Shim, D. Wang, T. Offerle, Investigation of factors affecting steering feel of column assist electric power steering, in: Dynamic Systems and Control Conference, Vol. 50701, American Society of Mechanical Engineers, 2016, V002T31A005.
[17] K. Johanastrom, C. Canudas-De-Wit, Revisiting the LuGre friction model, IEEE Control Syst. Mag. 28 (6) (2008) 101–114.
[18] S.H.M. Sadeghi, R. Sesana, D. Maffiodo, Friction calculation and simulation of column electric power steering system, Int. J. Mech. Mechatron. Eng. 11 (1) (2017) 153–160.
[19] S. Gao, X. Wang, Theoretical modeling and transmission characteristics analysis of a novel double-roller hourglass worm drive based on enveloping principle, Discov. Mech. Eng. 2 (1) (2023) 20.
[20] X. Su, D.R. Houser, Alternative equation of meshing for worm-gear drives and its application to determining undercutting and reverse engineering, J. Mech. Des. 122 (2) (2000) 207–212.
[21] C.-C. Liu, J.-H. Chen, C.-B. Tsay, Y. Ariga, Meshing simulations of the worm gear cut by a straight-edged flyblade and the ZK-type worm with a non-90° crossing angle, Mech. Mach. Theory 41 (8) (2006) 987–1002.
[22] K. Sharif, H. Evans, R. Snidle, Prediction of the wear pattern in worm gears, Wear 261 (5–6) (2006) 666–673.
[23] S. Mu, Y. Zhao, X. Zhang, Q. Meng, G. Li, Meshing theory of involute worm drive, Mech. Mach. Theory 165 (2021) 104425.
[24] F.L. Litvin, I. Gonzalez-Perez, K. Yukishima, A. Fuentes, K. Hayasaka, Design, simulation of meshing, and contact stresses for an improved worm gear drive, Mech. Mach. Theory 42 (8) (2007) 940–959.
[25] W. Predki, J. Hermes, Investigations on worm gears with the finite element method, Forsch. Ingenieurwesen 75 (2011) 93–105.
[26] L. Dong, P. Liu, W. Wei, X. Dong, H. Li, Study on ZI worm and helical gear drive with large transmission ratio, Mech. Mach. Theory 74 (2014) 299–309.
[27] D. Liang, C. Li, C. Hua, T. Luo, Experimental and numerical study of a plastic worm meshed with a steel helical gear, Trans. Can. Soc. Mech. Eng. 43 (3) (2019) 283–293.
[28] A.P. Shah, Y. Jadhav, Design, analysis and experimental study of worm and worm gear pair for plug valve application, Chin. J. Mech. Eng. (2020).
[29] X. Ye, Y. Chen, B. Lu, W. Luo, B. Chen, Study on a novel backlash-adjustable worm drive via the involute helical beveloid gear meshing with dual-lead involute cylindrical worm, Mech. Mach. Theory 167 (2022) 104466.
[30] V.V. Simon, Influence of tooth errors and shaft misalignments on loaded tooth contact in cylindrical worm gears, Mech. Mach. Theory 41 (6) (2006) 707–724.
[31] I. Seol, S. Chung, Design and simulation of meshing of new type of worm-gear drive with localized contacts, KSME Int. J. 14 (2000) 408–417.
[32] Q. Meng, Y. Zhao, Z. Yang, J. Cui, Meshing theory and error sensitivity of mismatched conical surface enveloping conical worm pair, Mech. Mach. Theory 145 (2020) 103681.
[33] Y. Chi, Y. Zhao, X. Zhu, G. Li, X. Chen, Mismatched gearing composed of hourglass worm and spur gear: meshing theory, tooth contact simulation, comprehensive design, Mech. Mach. Theory 174 (2022) 104883.
[34] Y. Hiltcher, M. Guingand, J.-P. de Vaujany, Load sharing of worm gear with a plastic wheel, J. Mech. Des. 129 (1) (2007) 23–30.
[35] A.E. Chakroun, C. Hammami, A. Hammami, A. De-Juan, F. Chaari, A. Fernandez, F. Viadero, M. Haddar, Gear mesh stiffness of polymer-metal spur gear system using generalized Maxwell model, Mech. Mach. Theory 175 (2022) 104934.
[36] F. Liu, Y. Chen, H. Xie, B. Lu, B. Chen, Study on the meshing stiffness of plastic helical gear meshing with metal worm via point-contact, Mech. Mach. Theory 176 (2022) 105040.
[37] C.G. Cooley, C. Liu, X. Dai, R.G. Parker, Gear tooth mesh stiffness: A comparison of calculation approaches, Mech. Mach. Theory 105 (2016) 540–553.
[38] C. Natali, M. Battarra, G. Dalpiaz, E. Mucchi, A critical review on FE-based methods for mesh stiffness estimation in spur gears, Mech. Mach. Theory 161 (2021) 104319.
[39] A.E. Chakroun, M. Battarra, E. Mucchi, The Bevel Local Slope Approach: A method for mesh stiffness estimation in spur, helical and spiral bevel gears, Simul. Model. Pr. Theory 139 (2025) 103047.
[40] S. Mu, X. Sun, Z. Dong, H. Yang, Y. Liu, W. Zhang, Q. Meng, Y. Zhao, Meshing theory of point-contact conical-envelope cylindrical worm-face worm gear drive, Mech. Mach. Theory 205 (2025) 105870.
[41] E. Bechhoefer, M. Kingsley, A review of time synchronous average algorithms, in: Annual Conference of the PHM Society, Vol. 1, 2009.